IMPACT AND SPREADING DYNAMICS OF A DROP OF FIBER SUSPENSION ON A SOLID SUBSTRATE

Sreeram Rajesh,[a] Alban Sauret[b,c]

ABSTRACT

Hypothesis: The presence of non-Brownian spherical particles dispersed in a liquid modifies the impact and spreading dynamics of a drop on a hydrophilic substrate. The difference in spreading dynamics is attributed to the increase in the viscosity of the suspension caused by the presence of the particles. Similarly, the presence of anisotropic non-Brownian particles, such as fibers, also increases the bulk viscosity of the suspension. In addition to the diameter D of the fiber, the length L, which determines the aspect ratio $A = L/D$, is crucial in controlling the viscosity of a fiber suspension. Therefore, we hypothesize that the drop impact of fiber suspensions with different volume fractions will result in a similar modification of the spreading dynamics.

Experiment: To investigate the impact and spreading dynamics, we prepare suspensions of fibers with an aspect ratio $A = 12$ at different volume fractions. These volume fractions span the dilute, semi-dilute, and dense concentration regimes. Additionally, we conduct a subset of experiments with aspect ratios $A = 4$ and $A = 20$. Furthermore, we characterize the thickness of the resulting droplet film, as well as the coating and orientation of fibers after the spreading dynamics reach a steady state.

Findings: The presence of fibers significantly influences the spreading dynamics and final size of the droplet on the hydrophilic substrate. Notably, the resulting droplet size after spreading decreases as the volume fraction of fibers in the suspension increases. To rationalize these results, we use a modified equation, originally developed for spherical particles, which incorporates the viscosity of the suspension. Additionally, we observe an increase in the splashing of the droplet during spreading when increasing the Weber number and the volume fraction. Furthermore, we show that as the volume fraction increases, the final thickness of the droplet increases, and the resulting fiber coating becomes less uniform. We also highlight the secondary influence of fiber geometry on the coatings, such as the overlap of fibers, which further affects the coating uniformity. Despite these geometry-induced modifications, the radial orientation of the fibers remains isotropic across all volume fractions considered in this study.

1 INTRODUCTION

The impact, spreading, and final deposition of liquid droplets on solid substrates are encountered in a wide range of natural and industrial situations, from raindrops falling on soil to suspension drops in inkjet printers. Various aspects of drop impact on solid surfaces have been studied, such as the early dynamics after contact, the role of substrate wettability, the maximum spreading diameter, the splashing threshold, or the force exerted on the substrate see, *e.g.*,[1,2]. Such studies have greatly improved our understanding of the impact of droplets of Newtonian fluids. However, many industrial processes involve capillary flows of complex fluids such as polymer solutions *e.g.*,[3–5], particulate suspensions *e.g.*,[6,7], and colloidal particles[8]. The numerous applications of drop impacts have motivated many recent studies with more complex rheology[9]. For instance, on the impact of shear thickening and shear thinning fluids on a hydrophobic surface[10], numerical simulations of the impact of viscoelastic liquid droplets[11], the impact of yield-stress fluids on a flat surface[12], and drop impact on thin films[13]. Such studies have extended our understanding of drop impact to homogeneous complex fluid systems.

However, studies investigating the effect of discrete particles during the impact and deposition of suspension drops on substrates remain scarce. This topic is important because the deposition of droplets of particulate suspensions occurs in processes such as inkjet printing[14,15], 3D printing of fiber composite matrices[16], and drug delivery to designated parts of the respiratory system[17]. The deposition of fiber particulates such as asbestos is also of environmental concern, as the pollutants can be deposited in the lungs see[18]. Past studies have considered the role of non-Brownian particles dispersed in a fluid during capillary flows. For instance, particles have been shown to modify the pinch-off of droplets[6,19–22] or thin-film coating processes[23–25]. The role of spherical, non-Brownian particles has also been inves-

---

[a] *Department of Mechanical Engineering, University of California, Santa Barbara, California 93106, USA; E-mail: sreeram@ucsb.edu*

[b] *Department of Mechanical Engineering, University of Maryland, College Park, Maryland 20742, USA; E-mail: asauret@umd.edu*

[c] *Department of Chemical Engineering, University of Maryland, College Park, Maryland 20742, USA*

tigated for the drop impact on flat surfaces[26–28], and on cylindrical targets[29]. The studies on drop impacts of particle-laden fluids have characterized the morphology of the suspension droplet upon impact, the splashing threshold, and the final particle distribution. However, the influence of anisotropic non-Brownian particles, such as fibers, during the impact, spreading, and coating of a suspension drop on a solid substrate has received much less attention and remains unclear. In the present study, we experimentally investigate the impact of a drop of fiber suspension on a hydrophilic glass surface to address these questions.

Interfacial flows of non-Brownian fiber suspensions exhibit complex multiphase dynamics arising from interactions between discrete fibers and the surrounding liquid-air interface[20,30]. In many industrial applications, capillary interactions of fibers play a crucial role[31,32]. When fibers are introduced at capillary scales, comparable to the characteristic length scale of the flow, their random packing within the liquid is modified, influencing the overall suspension dynamics. This is particularly pronounced at larger volume fractions, potentially inducing fiber ordering or resulting in fibers protruding through the liquid-air interface. In applications involving additive manufacturing and spray-coating, capillary interactions influence both the coated area and fiber orientation, which are crucial to material strength[33,34]. In bioprinting of organs, capillary-scale interactions of deformable anisotropic particles are relevant to cell extrusion, where precise cell alignment is essential[35]. Similarly, capillary-driven flows are also important in applications such as self-healing gels, localized drug release and delivery, fibrous porous water treatment membranes, and industrial-grade separations, where extrusion-based methods are used to deposit fibers and anisotropic particles[36–38]. Another well-studied example is capillarity-driven flows of particles toward the contact line during the evaporation of colloidal suspensions, affecting uniformity and coverage[39–41]. The present study aims to identify key quantities relevant to industrial applications involving the deposition of droplets of fiber suspensions and examine how parameters such as volume fraction and fiber geometry influence these quantities.

While the spreading dynamics, final droplet size, shape, and splashing threshold have been studied for spherical particles, the effects of fibers remain largely unexplored[26–28,42]. The approach used in this study successfully quantifies these parameters for fiber suspensions. Notably, we introduce the concept of area fraction to quantify the final surface area coated by the fibers following the droplet impact, enabling a description of the effects introduced by the presence of anisotropic particles within the droplet. Additionally, we develop an in-house routine to quantify the radial orientation of fibers in the deposited droplet, with the capability to distinguish overlapping fibers accurately. Our investigations provide a framework for quantifying key factors associated with capillary flows and interfacial effects in the droplet deposition of non-Brownian fiber suspensions. Importantly, we address a critical gap in the literature on droplet deposition involving anisotropic particles.

The paper is organized as follows: in §2, we present the experimental techniques used in this study. In §3.1, we discuss the dynamics of the droplet as it impacts and spreads on a surface, the resulting thickness of the deposited film, and map the splashing after the drop impact. Following this, we present a discussion on the coating of the deposited fibers and the distribution of their orientations in §3.4. We then draw concluding remarks in §4.

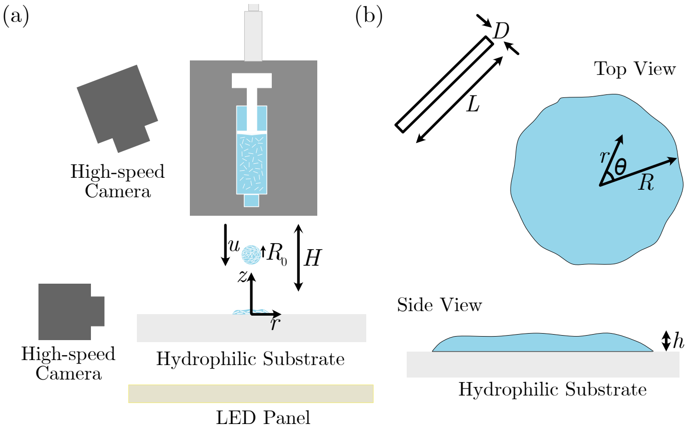

Figure 1: (a) Schematic of the experimental setup. (b) Top and side views of the geometry of the droplet as it spreads. The fibers have cylindrical cross-section of diameter D and a length L.

2 EXPERIMENTAL METHODS

The experimental setup, shown in figure 1(a), consists of a syringe filled with the fiber suspension mounted vertically on a micrometer translation stage. The quasi-static extrusion of the fiber suspension from a nozzle of diameter 3 mm leads to a pendant drop. The drop detaches when gravity overcomes the capillary forces, leading to droplets of diameter $d_0 = 2R_0 = 4 \pm 0.1$ mm. The droplet is released from a height $H = 10$, 14, and 18 cm, resulting in impact velocities $U = 1.4$, 1.65, and 1.9 m/s, and thus a timescale of impact $t_{\rm i} = d_0/U \approx 2$ - 4 ms. More details on the free-fall dynamics of the droplet are provided in §S1 of the supplementary material. To ensure consistent results, we performed seven realizations of the experiment for each parameter investigated. The substrate on which the droplet impacts is a hydrophilic glass surface. We prepare the substrate by polishing it with an abrasive compound (3M, Cerium Oxide), ensuring a consistent surface for all experiments and a small contact angle, smaller than 5° for the solvent considered.

The suspension is made of non-Brownian nylon fibers dispersed in a density-matched solvent made of a mixture of water and glycerol (40%/60% by weight) of density $\rho = 1152\,\mathrm{kg/m^3}$ (measured with Anton-Paar DMA 35), dynamic viscosity $\eta_{\rm f} = 9.5\,$mPa.s (measured with Anton Paar MCR 302), and surface tension $\gamma = 67\,$mN/m (measured with Attension Tensiometer). The solvent has a contact angle $\theta_{\rm c} < 5^{\circ}$ on the glass substrate. Note that the presence of particles does not modify the density or the surface tension of the suspension (See Ref.[43,44]). We disperse the nylon fibers of various aspect ratios $A = L/D$ at different volume fractions ϕ in the solvent. Most of the experiments are performed with fibers of diameter $D \approx 50\,\mu$m and length $L \approx 600\,\mu$m, resulting in $A = 12$. We also present some results for a smaller set of volume fractions for fibers of aspect ratios $A = 4$ and $A = 20$ and the same diameter $D = 50\,\mu$m (See figure S2 in supplementary materials for the size distribution of the fiber lengths). Overall, we use a volume fraction $\phi \in [0.1, 20]\%$, depending on the aspect ratio. Indeed, for too large aspect ratios or volume fraction, the fibers may clog the nozzle[45,46]. For the range of volume fractions used here, we ensured that the volume fraction of fibers in the extruded drop is similar to the volume fraction in the nozzle, *i.e.*, there is no self-filtration at the syringe nozzle[47] (see supplementary material, figure S3).

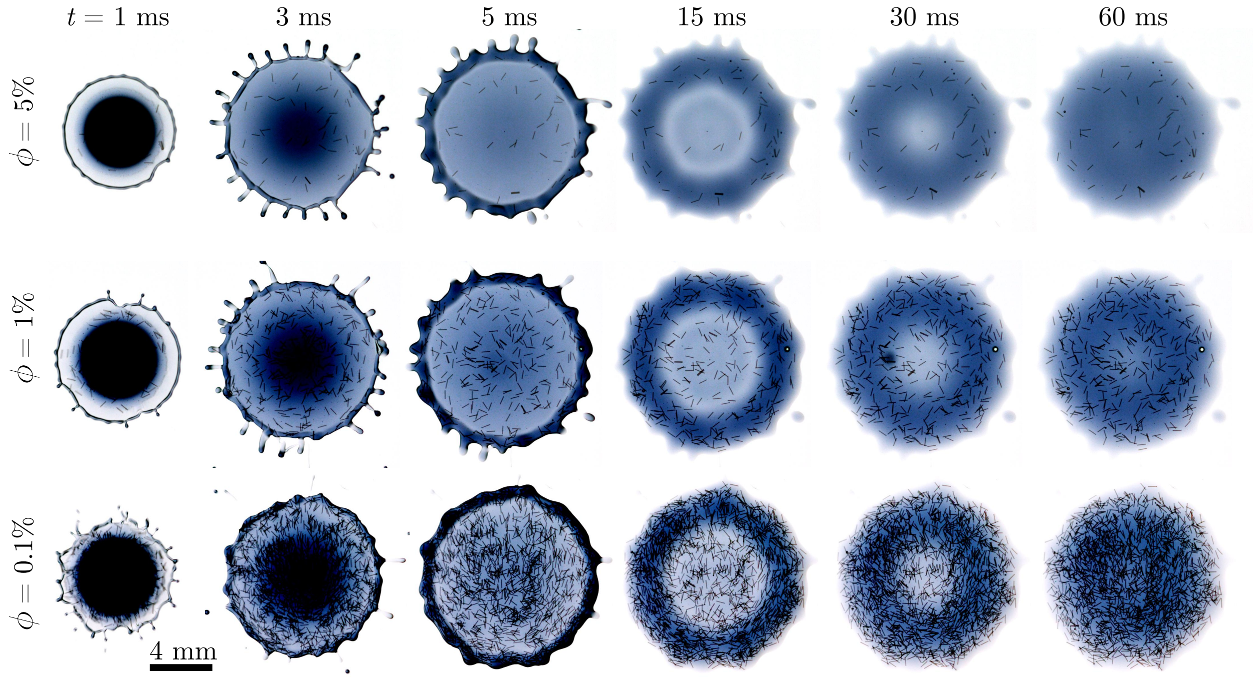

Figure 2: Snapshots of time-evolution of the suspension droplet upon impact for volume fraction $\phi = 0.1\%$, $\phi = 1\%$, and $\phi = 5\%$ for fibers of length $L = 600\,\mu$m and diameter $D = 50\,\mu$m.

In the present work, we considered moderate Weber numbers $\mathrm{We} = \rho U^2 d/\gamma = 135$, 190, and 240. The Reynolds number of the solvent droplet upon impact is defined as $\mathrm{Re_f} = \rho U d/\eta_\mathrm{f}$ and takes the values 680, 800, and 920. Alternatively, we could define a suspension Reynolds number as $\mathrm{Re}(\phi) = \rho U d/\eta(\phi) = \mathrm{Re_f}\,\eta_\mathrm{f}/\eta(\phi)$, where $\eta(\phi)$ is the viscosity of the fiber suspension. The impact and spreading dynamics are recorded from the top and the side at 10,000 frames per second (VEO Phantom 640), as shown in figure 2.

For an aspect ratio $A = 12$, the limits of the dilute, semi-dilute, and dense regimes are $\phi \ll 0.54\%$, $0.54\% \leq \phi \ll 6.5\%$, and $\phi \geq 6.5\%$, respectively, based on the limits provided by Butler *et al.*[48] (Further details provided in §S1, supplementary material). In the semi-dilute or dense regime, the hydrodynamic and fiber-fiber interactions cannot be neglected[49]. Different empirical correlations have been proposed to describe the viscosity of fiber suspensions $\eta(\phi)$. Here, in the range of volume fraction considered, we use the Maron-Pierce correlation, giving the steady-state shear viscosity of fiber suspension[50]:

$$\eta = \eta_0(1 - \phi/\phi_\mathrm{c})^{-2}, \tag{1}$$

where ϕ_c is the critical volume fraction at which the viscosity diverges, and depends on the fiber aspect ratio. We should emphasize that other empirical correlations would have been possible for the present fiber suspensions. For instance, Tapia *et al.*[51] proposes $\eta = \eta_0(1 - \phi/\phi_\mathrm{c})^{-0.9}$ for fibers of volume fraction $\phi > 25\%$. However, for the range of volume fraction considered here ($\phi \leq 10\%$), we use the Maron-Pierce correlation, similar to the range of ϕ explored by Bounoua *et al.*[50]. Further, the Maron-Pierce model has been previously found to work well to describe the dip-coating of substrates with fibers[32].

3 RESULTS AND DISCUSSION

3.1 SPREADING DYNAMICS OF FIBER SUSPENSIONS

3.1.1 INITIAL SPREADING OF THE SUSPENSION DROPLET

The droplet is released at a height H and impacts the substrate with a velocity U. Figure 3(a) shows the time-evolution of the rescaled radius $R(t)/R_0$ of the outer edge of the droplet for $A = 12$ and varying the volume fractions $\phi \in [0, 10]\%$ at $\mathrm{We} = 135$. We consider here the spreading dynamics of the droplet after the initial contact with the surface at $t = 0$ ms and until the radial spread reaches a steady-state value around $t \simeq 100$ ms. While the droplet continues to relax beyond this time, the increase in the droplet size is about 25% from the maximum droplet size over $t \simeq 30\,\mathrm{s} \gg 100$ ms. The long-term evolution of the drop is driven by capillarity and gravity, unlike the early-time inertia-driven spreading dynamics. Additionally, the evaporation of the solvent is also relevant for the long-term droplet size evolution ($t \geq 30$ s). Therefore, a detailed description of the long-term evolution of the drop is beyond the scope of the present study.

During the initial spreading, *i.e.*, for $t < t_\mathrm{coll}$, the radius $R(t)$ rapidly increases, as seen in the unshaded region in figure 3(a). Here, t_coll is the collision time defined as $t_\mathrm{coll} = 2R_0/U$[42,52]. The value of $t_\mathrm{coll} \approx 2.5$ ms for $\mathrm{We} = 135$ is shown by the dotted lines in figure 3(a). This timescale agrees well with our experimental observation of when the spreading radius R approaches a steady value. The evolution of the dimensionless radius $R(t)/R_0$ shows that the addition of fibers slightly slows down the initial spreading. Indeed, as we increase ϕ, the macroscopic viscosity $\eta(\phi)$ increases in the presence of particles, resulting in larger viscous dissipation.

The spreading velocity, non-dimensionally defined as V/V_coll,

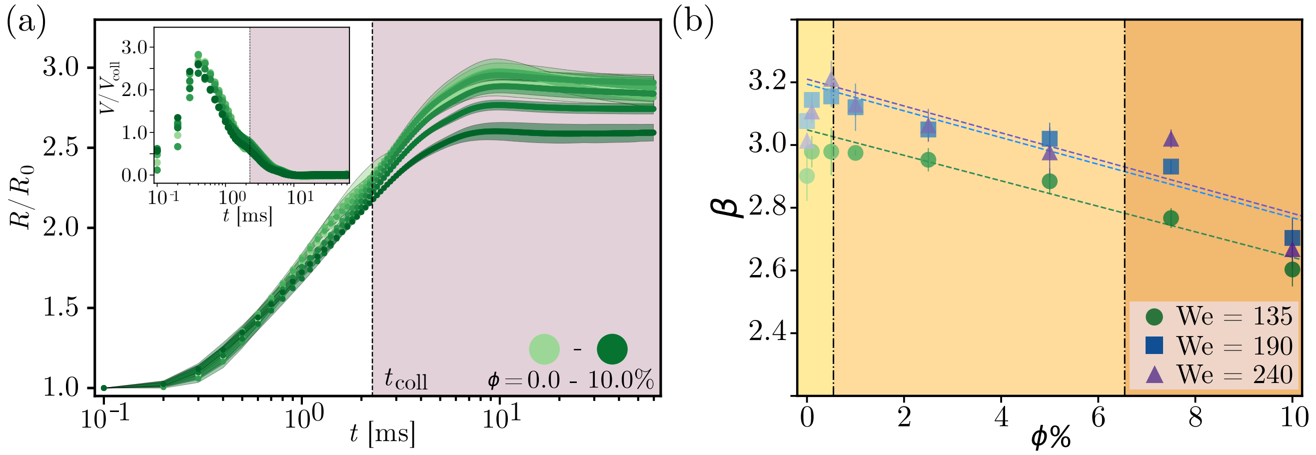

Figure 3: (a) Time evolution of the rescaled radius R/R_0 for varying volume fraction $\phi \in [0, 10]\,\%$ of fibers ($A = 12$) and We $= 150$. The shaded region shows the later stage of spreading once the droplet has fully impacted the surface ($t > t_{\rm coll}$). Inset: time-evolution of the rescaled spreading velocity $V/V_{\rm coll}$. (b) Spreading factor $\beta = \max(R/R_0)$ for suspensions of $A = 12$ fibers with $\phi \in [0, 10]\,\%$ and We $= 135 - 240$. The dashed lines indicate fits using equation 4. The colored regions indicate the dilute, semi-dilute, and dense regimes (from left to right)

where $V = {\rm d}R/{\rm d}t$ and $V_{\rm coll} = R_0/t_{\rm coll}$, is reported in the inset of figure 3(a) for the same experimental parameters as in the main panel. Following the impact, the spreading velocity reaches a peak before the spreading slows down due to viscous effects. The viscous dissipation arises from two contributions: wall friction on the substrate and the presence of particles. As expected, the peak velocity decreases slightly when increasing ϕ, due to the increase in macroscopic viscosity.

3.1.2 FINAL SPREADING RADIUS

After the collision ($t > t_{\rm coll}$), the droplet spreads to a maximum radius, as seen in figure 3(a), before slightly relaxing to a final shape for $t \gg t_{\rm coll}$. As the droplet spreads, the kinetic energy from the impact is dissipated through viscous effects, and R/R_0 plateaus toward a constant value. To quantify the influence of ϕ on the maximum spreading radius, we define the spreading factor $\beta = \max(R/R_0)$[26]. We report in figure 3(b) the evolution of β measured from our experiments for the $A = 12$ fibers at We $=$ 135, 190, and 240 and increasing volume fraction. The shaded regions from light to dark represent dilute, semi-dilute, and dense regimes[48]. In the dilute regime $0\% < \phi < 1\%$, we note that β slightly increases as volume fraction increases. However, in the semi-dilute and dense regimes, $\phi \gtrsim 1\%$, the final radius decreases as ϕ increases, as expected from the increase in viscous effects with ϕ. We also observe similar results for the $A = 4$ and $A = 20$ fibers at different We (figure S4 in the supplementary material).

We can try to rationalize the evolution of $\beta(\phi)$ using a model developed by Pasandideh *et al.*[42] for particle-free Newtonian liquids, and extended by Nicolas[26] for suspensions of neutrally buoyant spherical particles. When an initial suspension drop of volume $\Omega = 4\pi {R_0}^3/3$ impacts a solid substrate from a height H, the total energy of the drop just before the impact is purely due to the kinetic energy gained from the free fall, $E_{\rm K} = 4\pi\rho {R_0}^3 U^2/3$. After the impact, the spreading droplet dissipates energy through viscous losses, $W_{\rm d} = 4\,\alpha\,\pi\,\eta\,{R_0}^2\beta^4$, where α is a fitting parameter of order 1. Similar viscous dissipation controlling bounding and merging behavior has also been quantified for liquid droplets impacting on thin liquid films[53]. For the solvent, an energy balance provides the expression for the spreading factor[42]:

$$\beta = \left(\frac{{\rm Re}_{\rm f}}{12\alpha}\right)^{1/4} \tag{2}$$

For suspensions of particles, the Reynolds number ${\rm Re}(\phi)$ is related to the Reynolds number ${\rm Re}_{\rm f}$ of the solvent through ${\rm Re}(\phi) = {\rm Re}_{\rm f}/\eta_{\rm r}(\phi)$. As defined in equation 1, the relative viscosity is given by $\eta_{\rm r} = \eta(\phi)/\eta_0 = (1 - \phi/\phi_{\rm c})^{-2}$, such that the expression for the spreading factor for the droplet of fiber suspension becomes:

$$\beta = \left(\frac{{\rm Re}_{\rm f}}{12\alpha}\right)^{1/4} \left(1 - \frac{\phi}{\phi_{\rm c}}\right)^{1/2} \tag{3}$$

Furthermore, when $\phi \ll \phi_{\rm c}$ we can approximate equation 3 as a linear expression:

$$\beta = \left(\frac{{\rm Re}_{\rm f}}{12\alpha}\right)^{1/4} \left(1 - \frac{1}{2}\frac{\phi}{\phi_{\rm c}}\right) \tag{4}$$

We use equation 4 to fit β measured from the experiments, as shown in figure 3(b), which captures $\beta(\phi)$ well in the semi-dilute and dense regime (*i.e.*, $\phi > 1\%$) for $A = 12$ fibers at different We. For fibers, the maximum random packing fraction $\phi_{\rm c}$ depends on aspect ratio A (See Ref.[50]). For $A = 12$, we consider $\phi_{\rm c}=$ 37.5%, which provides the viscosity of the suspension in the range $\eta \in [9.5, 17.66]$ mPa.s for $\phi \in [0, 10]\%$, and a fitting parameter $\alpha \approx 0.76 \pm 0.03$ that depends weakly on We. Similar fits for the $A = 4$ and $A = 20$ fiber suspensions are provided in §S4 of the supplementary material. The values of $\phi_{\rm c}$ used here are based on estimates from the work of Bounoua *et al.*[50] and describe well the evolution of β measured in this study. Nevertheless, $\phi_{\rm c}$ remains an estimate, and detailed measurement of the rheology of fiber suspensions at different aspect ratios would allow us to obtain $\phi_{\rm c}(A)$.

The values of α estimated from our experiments are close to the values reported in Ref.[26] ($\alpha \approx 0.89$ for spherical particles on a hydrophilic solid substrate). The larger values of α observed for $A = 4$ and $A = 20$ noted in §S4 are likely due to a smaller

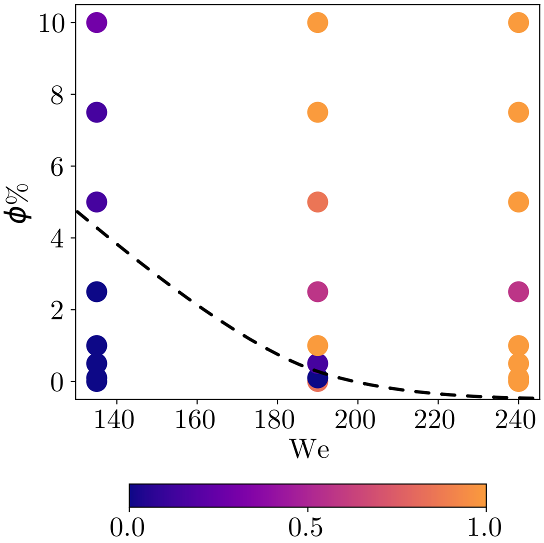

Figure 4: Diagram showing the splash/no splash regions for the $A = 12$ fibers as a function of ϕ and We. The color map corresponds to the normalized number of droplets ejected. The dashed lines are a guide for the eye, demarcating the splash/no splash boundary.

sample set of ϕ (only three values of ϕ were considered, as shown in figure S4). However, this confirms our hypothesis on the role of viscous dissipation $\eta(\phi)$ on the final size of the suspension droplet, despite the differences in aspect ratio A. In summary, at first order, the spreading behavior of the fiber suspension droplets on a hydrophilic substrate can be captured through the modification of the effective macroscopic viscosity, and one can neglect the local heterogeneity brought by the particles. This observation is reminiscent of the similar configuration with spherical particles. Therefore, the main effect of the geometry of the fibers here is to change the value of ϕ_c and, thus, the viscosity at a given volume fraction, and one can neglect the local heterogeneities brought by the fibers during this phase.

3.2 SPLASHING CRITERION FOR FIBER SUSPENSIONS

Understanding the splashing of suspension droplets is essential for good predictions of the final size and shape of the deposited droplet[1]. Various splash criteria relating the droplet Reynolds number, Re, and Weber number, We, have been proposed for a liquid impacting on a substrate[54,55]. Modified versions of these expressions have also been investigated for suspensions of spherical particles[27,56–58]. However, such models fail to capture the splash/no splash observations in the present study. A modified criterion for splashing in the drop impact of suspensions has been proposed by defining a particle-based Weber number[59]. However, this model does not address the role of ϕ.

In figure 4, we show the regime map for the splashing of $A = 12$ fibers with $\phi \in [0, 10\%]$. The color map corresponds to the normalized number of droplets ejected. The dashed lines are a guide for the eye, demarcating the splash/no splash boundary. As observed, the criterion not only depends on We and Re, but also on ϕ. At We = 135, we observe splashing only when $\phi > 2.5\%$. For $\phi > 2.5\%$, as ϕ increases, the number of droplets ejected also increases. The threshold decreases with We. For We = 190, we see splashing when $\phi = 0\%$ and for $\phi > 0.1\%$. At We = 240, we observe splashing for all values of ϕ. Similar splash/no splash observations have been previously reported for spherical particles[27], where splashing was observed with an increase in both We and ϕ. This work, however, did not describe the number of droplets ejected. We conclude from our observations that the splashing behavior of suspension droplets is influenced by multiple factors, including We, Re, and ϕ. For fiber suspensions, additional factors such as aspect ratio A may also modify this behavior. From a limited number of tests, we observe an increase in splashing with We for $A = 4$ and $A = 20$ fibers. However, a larger data set is necessary to build an accurate model on the influence of A on splashing and is beyond the scope of the study, where our primary focus is on the final deposited droplet. This is considered in the following sections.

3.3 FINAL THICKNESS PROFILE OF THE DROPLET

Quantifying and predicting the thickness profile of droplets on a surface is important in coating applications, inkjet printing, and additive manufacturing[15,33,60,61]. Various methods can be used to measure or estimate the thickness of the liquid film, such as imaging from the side or estimating the average thickness from the droplet weight and radius. Such methods, however, have the limitation that the thickness of the droplet can only be estimated along a fixed plane or on an average. An accurate way to measure the thickness for the entire drop is through a light absorption technique, where the intensity transmitted by a dyed liquid film is mapped to a previously calibrated thickness[62]. This technique was initially considered for pure liquid[62] and later used with suspensions of spherical particles[29]. Here, we adopt this technique for fiber suspensions.

Before we prepared the suspension, we added $1.2\,\mathrm{g\,L^{-1}}$ of Nigrosin (Sigma-Aldrich), a black-dye commonly used for biological samples, to the solvent. Nigrosin has been shown to not alter the surface tension or the viscosity of the liquid[63]. The details of the calibration and method are provided in §S5 of the supplementary material. The calibration allows us to convert the intensity I measured at any location and time by the high-speed camera to the local liquid thickness (from the calibration parameter and the reference intensity I_0). We show an example of the time evolution of the 3-dimensional thickness profile extracted from the procedure for a fiber suspension of volume fraction $\phi = 0.5\%$ and $A = 12$ in figure 5(a).

From our observations on droplet spreading dynamics, shown in figure 3(a), the droplet reaches a steady state of spreading around $t \simeq 100\,\mathrm{ms}$. Using the technique described previously, we extract the thickness profile of the droplet in this final state for $A = 12$ at different ϕ and We. We show the azimuthally averaged profiles for one realization of the experiment in figure 5(b) (solid green lines) for $0 \leq \phi \leq 10\%$ and We = 135. The shape of the droplets in this state can be described, at first order, as a spherical cap. This is a reasonable assumption since the maximum height of the droplets on the substrate is of order $h \sim 1\,\mathrm{mm}$, smaller than the capillary length $\ell_c = 2.3\,\mathrm{mm}$ and the Weber number is small. Hence, capillarity dominates. Note that such an assumption is expected to work well in the limit of vanishing Weber numbers and deviate at larger Weber numbers. The assumption of a spherical cap has been previously used to study

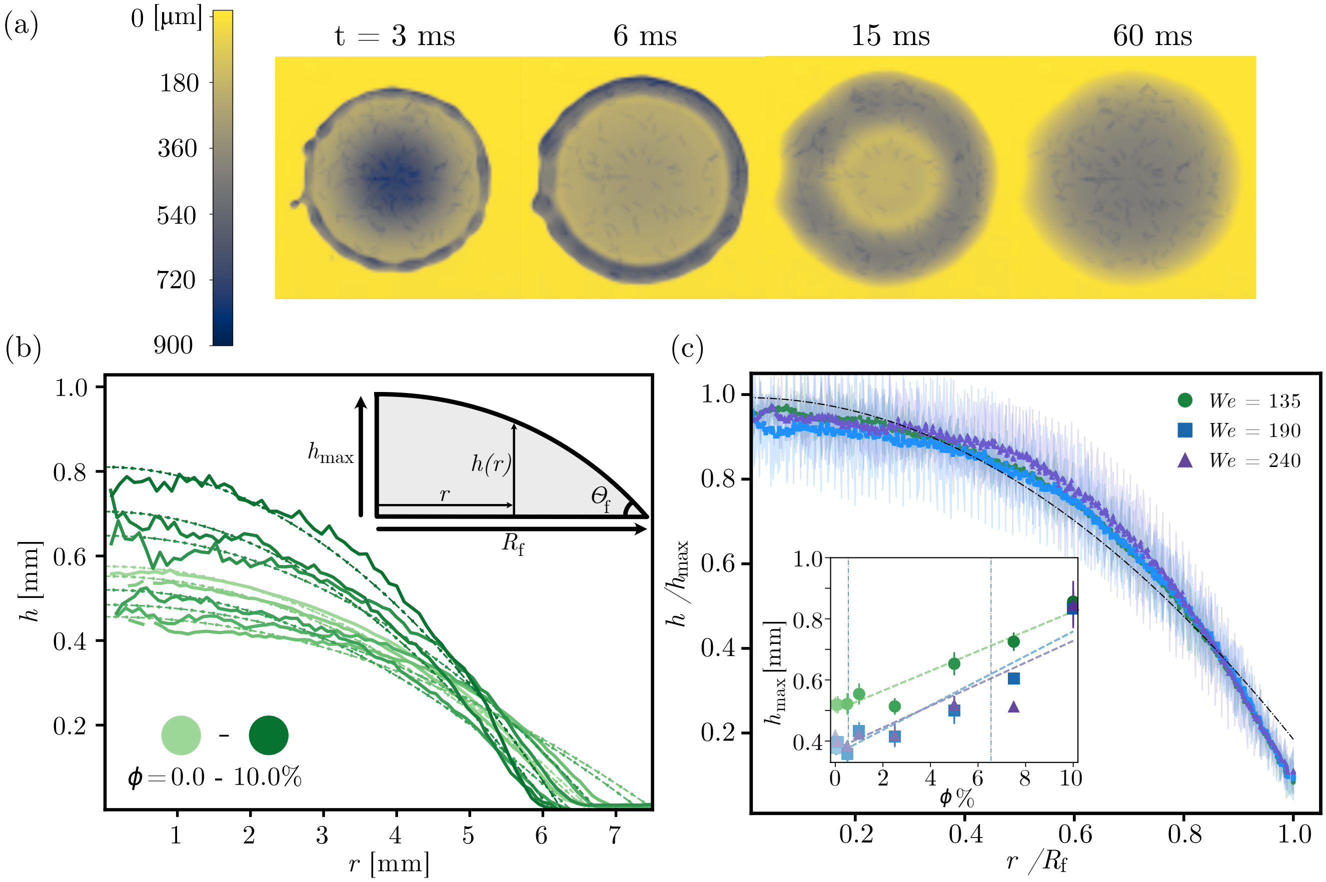

Figure 5: (a) Thickness profiles of a fiber suspension droplet of volume fraction $\phi = 0.5\%$ ($A = 12$) evaluated using absorption spectroscopy as it spreads on the substrate. (b) Final droplet thickness profiles (Solid green lines, $t \simeq 100\,\mathrm{ms}$) for suspensions of fibers of aspect ratio $A = 12$ and volume fractions $\phi \in [0 - 10]\,\%$ (from light to dark green) and We = 135. The dotted lines are fitted profiles, assuming the final profiles have the shape of a spherical cap (see Equation 5). Inset: Schematic of the steady-state droplet morphology and definition of the different physical quantities. (c) Rescaled mean thickness profiles for $A = 12$ fiber suspensions at different volume fractions. The solid lines show a smoothened signal overlaid on a shaded region with the raw mean thickness profile. Inset: Maximum thickness $h_{\rm max}(\phi)$ of the deposited droplet at different We. The error bars are obtained from five realizations of each experiment. The dotted lines are given by Eq. (6).

the evaporation of a sessile droplet deposited on a hydrophilic surface[39]. A schematic of the drop as a spherical cap is shown in the inset of figure 5(b). The equation for a spherical cap is:

$$h(r) = \left[\left(\frac{R_{\rm f}}{\sin \theta_{\rm f}} \right)^2 - r^2 \right]^{1/2} - \frac{R_{\rm f}}{\tan \theta_{\rm f}} \tag{5}$$

where $h(r)$ is the thickness of the droplet given as a function of the distance from the center $r = 0$, $R_{\rm f}$ and $\theta_{\rm f}$ are fitting parameters. The fit of the profile measured experimentally by equation (5) is shown by the dashed lines in figure 5(b) and is found to describe reasonably well the measured profiles. However, the experimental profile also exhibits a slightly squished droplet compared to a spherical cap. This is likely due to some flattening of the drop induced by inertia at impact and to some effects of gravity in the final state. The final deposit radius $R_{\rm f}$, which is a fitting parameter, is found to only differ slightly by less than 5% from the direct measurement R shown in figure 3(a). The contact angle for the different volume fractions is in the range $5^\circ \leq \theta_{\rm f} \leq 15^\circ$, and increases linearly with ϕ. This contact angle range is expected for a hydrophilic substrate, and the slight increase can be due to the presence of particles. In addition, these profiles only represent one realization of the experiment. We can thus consider that equation (5) works well to describe the steady-state thickness, except at the edge of the droplet, in this limit of small Weber numbers. We also observe in 5(b) that as ϕ increases, the final profile h of the droplet increases in the semi-dilute and dense regimes. This is consistent with what we observe in §3.1.1, where the radius of the drop decreases with increasing ϕ.

In figure 5(c), we show the rescaled mean thickness profiles $h/h_{\rm max}$ over the rescaled droplet radius $r/R_{\rm f}$ for $\phi = 0 - 10\%$ at We = 135, 190, and 240. We plot the mean thickness profile by averaging the thickness measured at different ϕ for a given We. We observe that the mean thickness profiles at different We are self-similar. The profiles are fitted using Equation 5, indicated by the dashed black lines. Hence, we use a single Equation to describe the steady-state thickness profile of a fiber suspension drop. The maximum droplet thickness $h_{\rm max}(\phi)$ is shown in the inset of figure 5(c). The error bars for $h_{\rm max}$ shown in the inset of Figure 5(c) are extracted from five realizations of an experiment for a particular ϕ, We, and A. As expected, $h_{\rm max}$ decreases slightly in the dilute regime before increasing with ϕ. To describe

$h_{\max}(\phi)$, we can use the conservation of volume, $R_0^3 \sim h_{\max} R^2$, equation 3, and a Taylor expansion to obtain:

$$h_{\max}(\phi) \propto R_0(1 + 0.5\phi/\phi_c) \tag{6}$$

Equation 6 is used to fit the measured $h_{\max}$ for the $A = 12$ fibers at different We, and is shown by the dashed lines in figure 5(c) inset.

3.4 SURFACE COVERAGE AREA OF FIBERS DEPOSITED

The final coating of fibers on a surface is relevant to applications from paints and coatings to surface functionalization, such as surface drag reduction[64,65]. In the top panel of figure 6(a), we show a top view of a drop of fiber suspension of $A = 12$ fibers with $\phi = 0.5\%$ and We = 135 at $t \simeq 100$ ms (*i.e.*, close to its final state after impact). We use image analysis to quantify the fraction of area ϕ_{area} of the substrate coated by the fibers in an annular region of the droplet for various volume fractions and report the results in figure 6(b) (for further details on the procedure used to measure ϕ_{area}, see §S6 in the supplementary material). The width of the annular region considered is $\Delta r = r_2 - r_1 = 0.5$ mm and taken at various distances r from the center of the droplet. The width, $\Delta r \approx L = 600\,\mu$m, and is kept constant in the present study. The volume fraction of fibers considered in figure 6(b) is $\phi = 0 - 10\%$. In the dilute regime ($\phi \in [0, 1]\%$), ϕ_{area} seems almost constant over the entire range of r. At first order, the result is a homogeneous surface coating of the fibers for all the Weber numbers we investigated (see supplementary figure S7 for We = 190 and We = 240 for $A = 12$ fibers, figure S8 for $A = 4$ fibers). For $\phi \geq 1\%$, as ϕ increases, there is a gradient in ϕ_{area} away from the center. We expect such an observation since the droplet has the shape of a spherical cap, and the thickness of the droplet decreases away from the center (see figure 5). This essentially results in a non-uniform coating at larger volume fractions. However, quantifying the area coated only provides a first-order description of the surface coverage by the fibers. Additional factors can be considered, such as the radial spread for different values of Δr, the overlap of the fibers, and their axial orientation within the capillary interface. Such second-order effects are unique to anisotropic particles since they can reduce the effective coated surface area. To explain our results on surface coverage, and the secondary effects unique to anisotropic particles, we first develop a model to capture ϕ_{area} as a function of the volume fraction ϕ. We then use this model to interpret experimentally measured ϕ_{area} and to quantify the secondary effects through a fitting parameter Ψ_1.

The area fraction ϕ_{area} occupied by the fibers in the annular region is the ratio of the apparent area of the fibers detected in the annulus to the total projected area of the annulus:

$$\phi_{\text{area}} = n_{\text{eff}} \frac{\Psi_1 D L}{\Delta S}, \tag{7}$$

where L and D are the length and diameter of the fibers, respectively, and Ψ_1 is a fitting factor that accounts for the apparent area detected. The projected area of the annular region, as shown in figure 6(a) is $\Delta S = \pi(r_2^2 - r_1^2)$. The effective number of fibers in the annulus, n_{eff}, can be calculated from the number of fibers per unit volume, n, and the volume of the annulus, $\Delta\Omega$, *i.e.*, $n_{\text{eff}} = n\,\Delta\Omega$. The volume in the annulus $\Delta\Omega = \Omega(r_2) - \Omega(r_1)$, where $\Omega(r)$ is the volume of a section of the spherical cap, and is given by:

$$\Omega(r) = \pi r^2 h(r) + \pi\left[h_{\max} - h(r)\right]\left[3r^2 + (h_{\max} - h(r))^2\right]$$

$h(r)$ is given by Equation 5. We also assume that the volume of liquid lost due to splashing is negligible for the parameters considered here.

Now that we have an expression for n_{eff}, we want to relate ϕ_{area} to the volume fraction ϕ. By definition, the volume fraction is:

$$\phi \approx N \frac{\Omega_{\text{fiber}} \rho_{\text{fiber}}}{\Omega_{\text{drop}} \rho_{\text{drop}}} \tag{8}$$

where N is the number of fibers in a drop, $\Omega_{\text{fiber}} = \pi D^2 L/4$ is the volume of a single fiber, ρ_{fiber} is the density of the fiber, and ρ_{drop} is the density of the suspension. As noted in §2, the fibers are neutrally buoyant in the solvent, hence $\rho_{\text{fiber}} \simeq \rho_{\text{drop}}$. Further, the number of fibers per unit volume can also be defined with respect to the volume of an undeformed drop, $n = N/\Omega_{\text{drop}}$. This simplifies the volume fraction to:

$$\phi \approx n \frac{\pi D^2 L}{4} \tag{9}$$

From equations (7) and (9), and using the fact that $n = n_{\text{eff}}/\Delta\Omega$, we get the expression for ϕ_{area} in terms of the volume fraction ϕ as:

$$\phi_{\text{area}} = \frac{4\,\Psi_1}{\pi D} \frac{\Delta\Omega}{\Delta S} \phi \tag{10}$$

As noted before, Ψ_1 is a fitting factor to account for the apparent area of the fibers captured using experiments. This factor provides second-order information on the area coated by the fibers. In addition to Ψ_1, we consider an additional term Ψ_2 to equation (10), which accounts for the effect of the squishing of the drop after impact due to both inertia and gravity. This results in a drop that is not a perfect spherical-cap, which is also noticeable as deformations at the edge in figure 5 (b). This deformation is not well represented by equation 10, has been discussed further in §S9 of the supplementary material. This provides the final expression for the area fraction in terms of volume fraction:

$$\phi_{\text{area}} = \frac{4\Psi_1}{\pi D} \frac{\Delta\Omega}{\Delta S} \phi + \Psi_2 \tag{11}$$

An interesting observation from this model is that ϕ_{area} is independent of the fiber length, L, for neutrally buoyant suspensions. This is not directly observable from experiments. We fit the model given by equation (11) to our experimental data shown in figure 6(b) and observe a reasonably good fit for our results. Further, the fitting parameter $\Psi 2$ measured for the $A = 12$ fibers are provided in figure S9 (b) in the supplementary material.

The values of Ψ_1 evaluated from ϕ_{area} for various ϕ at We = 135, 190, and 240 are shown in the inset of figure 6(b). We observe that Ψ_1 increases in the dilute regime but gradually asymptotes to a constant in the semi-dilute and dense regimes. The parameter Ψ_1 accounts for second-order effects introduced by the presence of fibers due to multiple factors such as overlapping, axial orientation for the fiber within the droplet, or the length of the region Δr considered. Factors such as overlapping and orientation of the fiber with respect to the vertical axis essentially result in less of the fiber area exposed. Additional factors, such as the size of the annular region Δr, could also introduce second-order effects. For instance, although the resulting coating is uniform at low volume fractions, certain regions of Δr may lack fibers entirely. This is reflected in the measured values of Ψ_1 for $0.1\% \leq \phi \leq 1\%$, which vary within the range $\Psi_1 \in [0.5, 2]$. For $\phi \geq 2.5\%$, the area covered by the fibers spans the entire droplet, eliminating non-uniformity across Δr. However, capillary effects induced by the droplet's shape lead to a weak decrease in Ψ_1, and

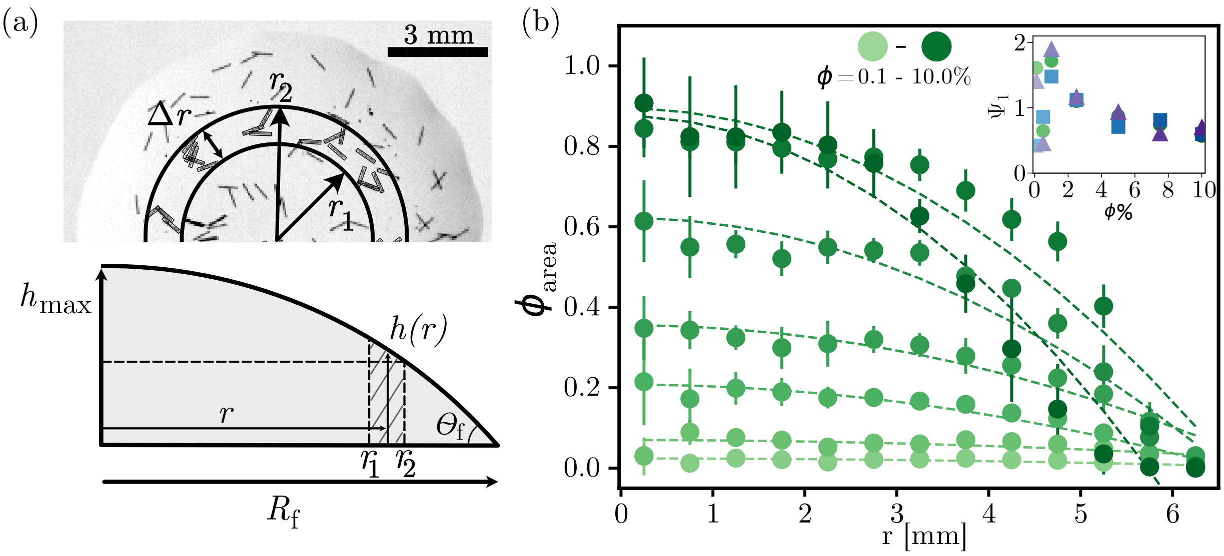

Figure 6: (a) Top: Snapshot of a drop of fiber suspension with $A = 12$ and $\phi = 0.5\%$ impacted at We = 135 at its final state. Bottom: Side-view schematic of the droplet at its final state. The shaded region represents the annulus within which the fraction of area occupied by the fibers is measured. (b) Annular area fraction ϕ_{area} at different radial distance r from the droplet center for $A = 12$ fibers and $\phi = 0 - 10\%$ at We = 135. The dashed lines show the fit using Equation 11. The fitting parameter Ψ_1 is shown in the inset for We = 135 (green circles), We = 190 (blue squares) and We = 240 (purple triangles).

results in a non-uniform coating of the fibers. To investigate this parameter further, we conducted additional experiments using fibers with $A = 4$, as reported in figure S8 in the supplementary material. Preliminary observations of Ψ_1 suggest it may be a non-linear function of multiple parameters, including ϕ, Δr, A, and capillary effects associated with the pinning of the contact line at the droplet boundary. Hence, further investigations are required to fully understand this parameter.

3.5 FINAL ORIENTATION OF THE FIBER

Capillary dynamics can play a crucial role in influencing fiber orientation during droplet deposition, as the balance of surface tension, inertia, and viscous dissipation aligns fibers in the suspension[40,66]. This alignment critically affects the mechanical, thermal, and functional properties of the resulting material, making it relevant to applications in industries such as additive manufacturing and biomedical engineering[67,68]. Further, the radial orientation is also required to calculate the deviatoric stresses in suspensions of anisotropic particles (see, e.g., the work by Shaqfeh and Fredrickson[49] for more details).

In the present study, we can directly measure the radial orientation θ_R in the dilute and semi-dilute regimes, where overlapping fibers remain distinguishable. We define θ_R as the angle formed between the fiber and the radial vector r passing through its center, as illustrated in figure 7(a). In figure 7(b)-(d), we summarize the measured values of θ_R after the droplet has reached its final state, *i.e.*, $t \simeq 100\,\text{ms}$. We measure this orientation for $A = 12$ fibers with $\phi \in [0.1, 5]\%$, $A = 4$ fibers with $\phi = 2\%$, and $A = 20$ fibers with $\phi = 0.4\%$, at We $= 135 - 240$. The procedure involves using a custom routine developed in Python that can distinguish between two overlapping fibers (see §S10 in the supplementary material).

In figure 7(b)-(d), we present the fraction of fibers detected as a function of θ_R. The distribution is based on seven experimental realizations for each parameter set, resulting in a dataset that ranges from over 100 to 5,000 points, depending on the value of ϕ. Figure 7(b) shows the orientation measured for $\phi = 0.1\%$ of the $A = 12$ fibers at We = 135, 190, and 240. In this dilute regime, we observe a slight anisotropy in the distribution of θ_R. Figure 7(c) captures the influence of volume fraction in the range $\phi \in [0.1, 5]\%$ for the $A = 12$ fibers at We = 135. Indeed, as ϕ increases, we observe that the distribution of θ_R becomes homogeneous, *i.e.*, the fibers are increasingly randomly distributed. This could be due to an increase in fiber-fiber interactions or an increase in viscous dissipation, which minimizes the rearrangement of fibers in any preferred direction. In figure 7(d), We probe the role of fiber geometry A, for aspect ratios $A = 4$, 12, and 20. We chose the volume fraction ϕ for different A such that we have sufficient fibers to quantify and that the suspensions have similar enough viscosity. Once again, we see an isotropic distribution for $\theta_R(A)$. The isotropy appears to decrease weakly with A. This observation suggests that of the two factors driving isotropy, *i.e.*, viscous dissipation and fiber-fiber interaction, the latter is likely more important. In summary, from figure 7(b)-(d), we note that the distribution of θ_R is within a narrow range of 0 to 0.1 across different We, ϕ, and A. Despite the slight differences observed, the overall steady-state radial orientation is isotropic across the range of parameters we measure.

Figure 7(b)-(d) provides insight into the net distribution of θ_R. However, it does not reveal any information on the distribution of θ_R in the radial or angular direction. To probe this, we quantify the distribution of θ_R as a function of r and θ. This is shown in figure 7(e) for a suspension with $\phi = 0.1\%$ and We = 135, 190, and 240. The heat map provides information on radial or angular preference for the distribution of θ_R, if any. However, figure 7(e) does not reveal any such preferential orientation. We observe this to be true for all the We across $\phi \in [0.1, 5]\,\%$ for the $A = 12$ fibers.

To summarize the radial orientations measured in figure 7(b)-

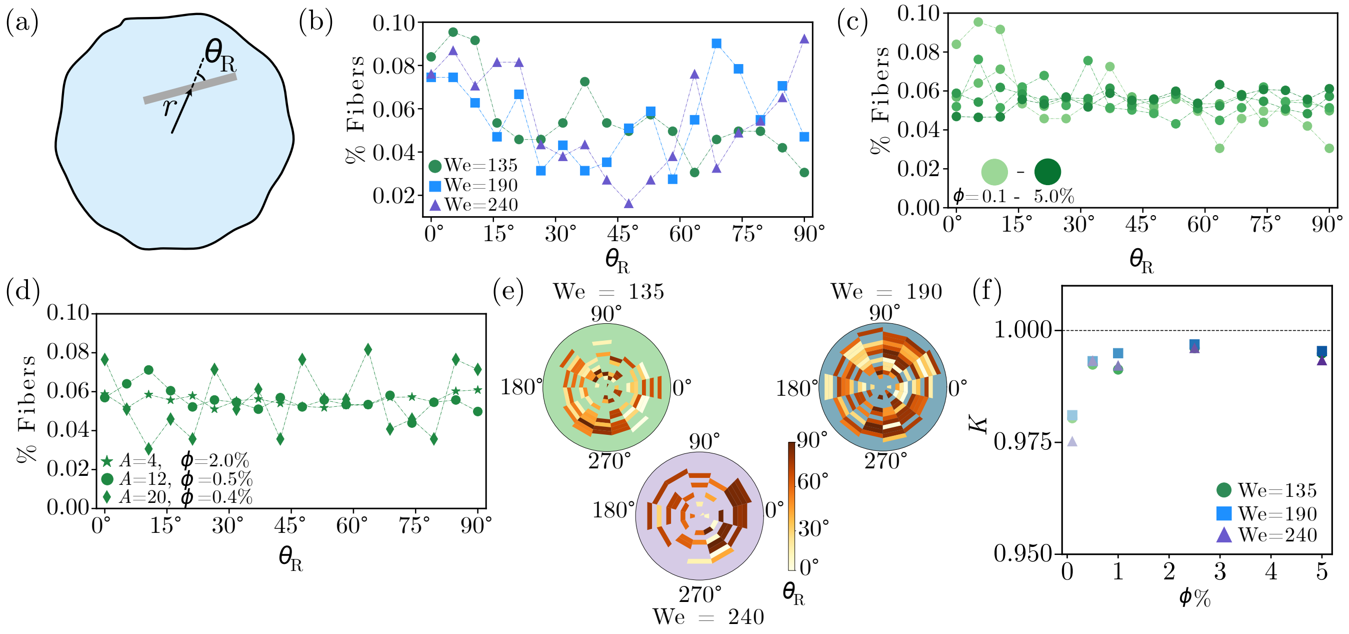

Figure 7: (a) Schematic of a droplet with a single fiber. The radial orientation is defined as θ_{R}, the angle the fiber makes with respect to the radial direction r through the center of the fiber. (b) Distribution of θ_{R} for $A = 12$, $\phi = 0.1\%$ fibers at We $= 135$, 190, and 240. (c) Distribution of θ_{R} for $\phi \in [0.1, 5]\,\%$ of $A = 12$ fibers at We $= 135$ (d) Distribution of θ_{R} for $A = 4, \phi = 2\%$ (star), $A = 12, \phi = 0.5\%$ (circle), $A = 20, \phi = 0.4\%$ (diamond) at We $= 135$. The dotted lines in figures (b)-(d) are only guides for the eye. (e) Heat map describing the radial spread of θ_{R} for $A = 12$, $\phi = 0.1\%$ at We $= 135, 190,$ and 240, corresponding to green, blue, and purple background, respectively. (f) Isotropy factor K for different values of ϕ for $A = 12$ fibers.

(d), we introduce an isotropy factor K. At a particular ϕ, We, and A, we define it as $K = 1 - \sigma$, where σ is the standard deviation of the distribution of θ_{R}. Hence, $K = 1$ here represents an isotropic distribution. We quantify the isotropy K as a function of ϕ in figure 7(f). The fibers considered are $A = 12$ with $\phi \in [0.1, 5]\,\%$ at We $= 135$, 190, and 240. As ϕ increases, K converges to 1. Hence, despite the narrow range K, we observe that as the volume fraction increases, the randomness in the distribution converges to 1. Similarly, we report the influence of fiber geometry A on the measured isotropy in figure S11 in the supplementary material. In summary, the quantification of K confirms that for the range of ϕ, We, and A considered in this study, the deposited fibers in the suspension exhibit weak to no preferential orientation. We mention here that during the dynamic spreading of the droplet, there is some preferential alignment for the droplet, initially in the radial direction, and perpendicular to the radius when the liquid forms a crest at the edge of the droplet (see Movie 1 and Movie 2). However, this orientation is simply the alignment of the fibers during the spreading, and as the spreading approaches steady-state, the θ_{R} distribution becomes isotropic.

4 CONCLUSION

The present study investigated the impact of a drop of fiber suspension on a hydrophilic substrate. The parameters explored include fibers of different volume fractions ϕ spanning the dilute, semi-dilute, and dense regimes. The droplets were released from various heights, resulting in different We and Re. While most of the experiments used fibers with an aspect ratio $A = 12$, a few additional experiments were conducted with $A = 4$ and $A = 20$ fibers to extend the broad parameter space.

We quantified several key features typically considered in studies on droplet impact: the spreading dynamics and maximum radius of the droplet [26,27], the steady-state thickness of the drop [29], the resulting coating of the fibers [69,70], and the steady-state radial orientation [32,64,71]. For our investigations on spreading dynamics and final droplet size, we hypothesized that as the volume fraction increases, the resulting size of the drop decreases due to the increase in apparent viscosity. This is indeed seen in our results for the fibers in semi-dilute and dense regimes. Further, the decrease in droplet radius implies that the droplet thickness $h_{\max}$ should increase with ϕ. We verified this by implementing an image spectroscopy technique for measuring the thickness of fiber suspensions.

Interfacial effects play a crucial role in determining the surface area coated by particles during droplet deposition, for instance, by controlling the release of particles during extrusion or spreading of gels used in self-healing materials [33,36], or by driving the flow of particles toward the contact line through capillary flow during the evaporation of colloidal suspensions [39]. This phenomenon, influenced by particle size, surface tension, and drying dynamics, is critical in applications like printing, coatings, and biomedical devices [40,41]. To analyze the fiber coating, we define ϕ_{area} as the surface area coated by the fibers. The analysis revealed that at low ϕ, the resulting coating seems uniform at first order, while at higher ϕ, it becomes inhomogeneous. Predicting the surface coating without experiments is challenging due to the anisotropic nature of the particles. A key difference between spherical particles and fibers is that fibers can overlap, especially at larger A. This introduces non-linear secondary effects that depend on multiple parameters such as the aspect ratio A, the volume fraction ϕ, and the annular region Δr considered. A description the coated area is essential to improve predictive capabilities for additive manufacturing or spray coating applications involving capillary deposition[33,34], since the surface area coated is critical to the strength of the material. We propose a model to capture the evolution of the coated area, $\phi_{\mathrm{area}}(r)$, which includes a fitting parameter, Ψ_1, to describe the second-order effects introduced by the fibers.

Capillary interfaces influence fiber orientation due to flow dynamics generated by the balance of surface tension, inertia, and viscous dissipation, resulting in fiber alignment during wetting, drying, and deposition processes[40,66]. The resulting fiber orientation critically influences the mechanical, thermal, and functional properties of materials, enhancing strength, conductivity, and porous media flows in industries like aerospace, automotive, and biomedical engineering[38,67,68,72]. Applications range from improving structural properties in 3D-printed composites, filtration systems, energy efficiency, and tissue scaffolds through precise alignment strategies See Refs.[37,72–74]. Our measurements of the radial orientation, θ_{R}, reveal that despite the different ϕ, We, and A explored, the resulting θ_{R} is isotropic. Hence, for the range of parameters considered here, the droplet impact process does not introduce any preferential orientation. Such an observation is useful in designing processes where uniform spreading of the fibers is necessary. The image analysis routine we developed to measure the orientations improves upon previous approaches by being able to distinguish between overlapping fibers with reasonable accuracy[32,71]. While the presented routine has its limitations arising from the accuracy of the segmentation routine used, introducing such an approach is crucial to measure θ_{R} at higher volume fractions.

Characterizing the capillary dynamics of suspension flow is complex but important for practical coating and industrial applications. The fiber suspensions considered here introduce additional complexity compared to spherical particles. Further studies are required to control the orientation of the fibers on the substrate, for instance, by laterally impacting suspension droplets. Nevertheless, we revealed key insights into the peculiar capillary dynamics of fiber suspensions that could aid in predictions for industrial processes. While the present study aims to discuss some first results on the drop impact of fiber suspensions, many future directions remain to be explored as capillary flows of fiber suspensions have not yet been as studied as well as capillary flows of spherical particle suspensions. In this work, investigations on the role of the aspect ratio A were limited. For studying the final size of the droplet, further experiments with different aspect ratios would refine the model for the fitting parameter α as a function of A. Similar studies could explore the role of A on droplet thickness h using the image spectroscopy technique we presented. Additionally, the technique can resolve dynamic droplet thickness and quantify the role of fibers in modifying capillary waves, such as during droplet spreading. Further investigations are also needed to probe the role of substrate wettability and orientation, which may be critical for designing 3D scaffolds or targeted drug delivery using droplet extrusion. Another important direction is to investigate if one could introduce a preferential orientation for such fibers deposited by drop impact, for instance, by controlling the orientation of the substrate or the nozzle or by freezing the droplet during the spreading stage to arrest the dynamic orientation of the fibers in motion.

Declaration of Competing Interest

The authors declare that they have no known competing financial interests or personal relationships that could have appeared to influence the work reported in this paper.

Acknowledgments

This material is based upon work supported by the National Science Foundation under NSF CAREER Program Award CBET Grant No. 1944844.

References

[1] C. Josserand and S. T. Thoroddsen, *Annual review of fluid mechanics*, 2016, **48**, 365–391.

[2] X. Cheng, T.-P. Sun and L. Gordillo, *Annual Review of Fluid Mechanics*, 2022, **54**, 57–81.

[3] M. A. Fardin, M. Hautefeuille and V. Sharma, *Soft Matter*, 2022, **18**, 3291–3303.

[4] S. Rajesh, V. Thiévenaz and A. Sauret, *Soft matter*, 2022, **18**, 3147–3156.

[5] S. Rajesh, S. S. Peddada, V. Thiévenaz and A. Sauret, *Journal of Non-Newtonian Fluid Mechanics*, 2022, **310**, 104921.

[6] R. J. Furbank and J. F. Morris, *Physics of Fluids*, 2004, **16**, 1777–1790.

[7] V. Thiévenaz and A. Sauret, *Proceedings of the National Academy of Sciences*, 2022, **119**, e2120893119.

[8] V. Bertola and M. D. Haw, *Powder technology*, 2015, **270**, 412–417.

[9] P. Shah and M. M. Driscoll, *Soft Matter*, 2024.

[10] M. Guémas, Á. G. Marín and D. Lohse, *Soft Matter*, 2012, **8**, 10725–10731.

[11] Y. Wang, M. Do-Quang and G. Amberg, *Journal of Non-Newtonian Fluid Mechanics*, 2017, **243**, 38–46.

[12] L.-H. Luu and Y. Forterre, *Journal of Fluid Mechanics*, 2009, **632**, 301–327.

[13] S. Sen, A. G. Morales and R. H. Ewoldt, *Journal of Fluid Mechanics*, 2020, **891**, A27.

[14] E. Tekin, P. J. Smith and U. S. Schubert, *Soft matter*, 2008, **4**, 703–713.

[15] D. Lohse, *Annual review of fluid mechanics*, 2022, **54**, 349–382.

[16] P. Parandoush and D. Lin, *Composite Structures*, 2017, **182**, 36–53.

[17] C. López-Iglesias, A. M. Casielles, A. Altay, R. Bettini, C. Alvarez-Lorenzo and C. A. García-González, *Chemical Engineering Journal*, 2019, **357**, 559–566.

[18] B. Asgharian and C. Yu, *Journal of aerosol science*, 1989, **20**, 355–366.

[19] C. Bonnoit, T. Bertrand, E. Clément and A. Lindner, *Physics of Fluids*, 2012, **24**, year.

[20] J. Château, É. Guazzelli and H. Lhuissier, *Journal of Fluid Mechanics*, 2018, **852**, 178–198.

[21] V. Thiévenaz and A. Sauret, *Physical Review Fluids*, 2021, **6**, L062301.

[22] V. Thiévenaz, S. Rajesh and A. Sauret, *Soft matter*, 2021, **17**, 6202–6211.

[23] A. Gans, E. Dressaire, B. Colnet, G. Saingier, M. Z. Bazant and A. Sauret, *Soft matter*, 2019, **15**, 252–261.

[24] D.-H. Jeong, M. K. H. Lee, V. Thiévenaz, M. Z. Bazant and A. Sauret, *Journal of Fluid Mechanics*, 2022, **936**, A36.

[25] D.-H. Jeong, L. Xing, J.-B. Boutin and A. Sauret, *Soft Matter*, 2022, **18**, 8124–8133.

[26] M. Nicolas, *Journal of Fluid Mechanics*, 2005, **545**, 271–280.

[27] V. Grishaev, C. S. Iorio, F. Dubois and A. Amirfazli, *Langmuir*, 2015, **31**, 9833–9844.

[28] V. Grishaev, C. S. Iorio, F. Dubois and A. Amirfazli, *Journal of colloid and interface science*, 2017, **490**, 108–118.

[29] P. S. Raux, A. Troger, P. Jop and A. Sauret, *Physical Review Fluids*, 2020, **5**, 044004.

[30] M. J. Solomon and P. T. Spicer, *Soft Matter*, 2010, **6**, 1391–1400.

[31] G. G. Fuller and J. Vermant, *Annual review of chemical and biomolecular engineering*, 2012, **3**, 519–543.

[32] D.-H. Jeong, L. Xing, M. K. H. Lee, N. Vani and A. Sauret, *Journal of Colloid and Interface Science*, 2023, **650**, 407–415.

[33] R. L. Truby and J. A. Lewis, *Nature*, 2016, **540**, 371–378.

[34] R. Turton and X. X. Cheng, *Powder Technology*, 2005, **150**, 78–85.

[35] S. V. Murphy and A. Atala, *Nature biotechnology*, 2014, **32**, 773–785.

[36] I. L. Hia, P. Pasbakhsh, E.-S. Chan and S.-P. Chai, *Scientific reports*, 2016, **6**, 34674.

[37] M. F. Haase, H. Jeon, N. Hough, J. H. Kim, K. J. Stebe and D. Lee, *Nature communications*, 2017, **8**, 1234.

[38] M. L. Wang, P. Yeon, C. F. Chamberlayne, M. Mofidfar, H. Xu, J. P. Annes, R. N. Zare and A. Arbabian, 2021 IEEE biomedical circuits and systems conference (BioCAS), 2021, pp. 1–4.

[39] H. Hu and R. G. Larson, *The Journal of Physical Chemistry B*, 2002, **106**, 1334–1344.

[40] R. D. Deegan, O. Bakajin, T. F. Dupont, G. Huber, S. R. Nagel and T. A. Witten, *Nature*, 1997, **389**, 827–829.

[41] E. R. Dufresne, E. I. Corwin, N. A. Greenblatt, J. Ashmore, D. Y. Wang, A. D. Dinsmore, J.-X. Cheng, X. S. Xie, J. W. Hutchinson and D. A. Weitz, *Physical Review Letters*, 2003, **91**, 224501.

[42] M. Pasandideh-Fard, Y. Qiao, S. Chandra and J. Mostaghimi, *Physics of fluids*, 1996, **8**, 650–659.

[43] A. Pelosse, É. Guazzelli and M. Roché, *Journal of Fluid Mechanics*, 2023, **955**, A7.

[44] É. Couturier, F. Boyer, O. Pouliquen and É. Guazzelli, *Journal of Fluid Mechanics*, 2011, **686**, 26–39.

[45] B. P. Croom, A. Abbott, J. W. Kemp, L. Rueschhoff, L. Smieska, A. Woll, S. Stoupin and H. Koerner, *Additive Manufacturing*, 2021, **37**, 101701.

[46] B. Dincau, E. Dressaire and A. Sauret, *Physics Today*, 2023, **76**, 24–30.

[47] M. Haw, *Physical review letters*, 2004, **92**, 185506.

[48] J. E. Butler and B. Snook, *Annual Review of Fluid Mechanics*, 2018, **50**, 299–318.

[49] E. S. Shaqfeh and G. H. Fredrickson, *Physics of Fluids A: Fluid Dynamics*, 1990, **2**, 7–24.

[50] S. N. Bounoua, P. Kuzhir and E. Lemaire, *Journal of Rheology*, 2019, **63**, 785–798.

[51] F. Tapia, S. Shaikh, J. E. Butler, O. Pouliquen and É. Guazzelli, *Journal of Fluid Mechanics*, 2017, **827**, R5.

[52] J. Eggers, M. A. Fontelos, C. Josserand and S. Zaleski, *Physics of fluids*, 2010, **22**, year.

[53] X. Tang, A. Saha, C. K. Law and C. Sun, *Langmuir*, 2018, **34**, 2654–2662.

[54] A. Moreira, A. Moita and M. Panao, *Progress in energy and combustion science*, 2010, **36**, 554–580.

[55] M. Marengo, C. Antonini, I. V. Roisman and C. Tropea, *Current Opinion in Colloid & Interface Science*, 2011, **16**, 292–302.

[56] A. L. Yarin, *Annu. Rev. Fluid Mech.*, 2006, **38**, 159–192.

[57] C. Mundo, M. Sommerfeld and C. Tropea, *International journal of multiphase flow*, 1995, **21**, 151–173.

[58] G. E. Cossali, A. Coghe and M. Marengo, *Experiments in fluids*, 1997, **22**, 463–472.

[59] I. R. Peters, Q. Xu and H. M. Jaeger, *Physical review letters*, 2013, **111**, 028301.

[60] A. Sauret, A. Gans, B. Colnet, G. Saingier, M. Z. Bazant and E. Dressaire, *Physical Review Fluids*, 2019, **4**, 054303.

[61] A. E. Siemenn, E. Shaulsky, M. Beveridge, T. Buonassisi, S. M. Hashmi and I. Drori, *ACS Applied Materials & Interfaces*, 2022, **14**, 4668–4679.

[62] C. Vernay, L. Ramos and C. Ligoure, *Journal of Fluid Mechanics*, 2015, **764**, 428–444.

[63] Y. Wang and L. Bourouiba, *Journal of Fluid Mechanics*, 2017, **814**, 510–534.

[64] R. Blell, X. Lin, T. Lindstrom, M. Ankerfors, M. Pauly, O. Felix and G. Decher, *ACS nano*, 2017, **11**, 84–94.

[65] M. Hasegawa and H. Sakaue, *Sensors and Actuators A: Physical*, 2020, **312**, 112125.

[66] A. L. Yarin and D. A. Weiss, *Journal of Fluid Mechanics*, 2006, **549**, 173–192.

[67] M. Jawaid, M. T. H. Sultan and N. Saba, *Structural health monitoring of biocomposites, fibre-reinforced composites and hybrid composites*, Woodhead Publishing, 2018.

[68] L. A. Pilato and M. J. Michno, *Advanced composite materials*, Springer Science & Business Media, 2013.

[69] Q. Xie, T. Du, C. J. Brabec and J. Harting, *arXiv preprint arXiv:2501.05088*, 2025.

[70] J. Maddox and A. Sauret, *Physical Review Applied*, 2024, **22**, 034071.

[71] S. Pashazadeh, A. S. Suresh, V. Ghai, T. Moberg, A. Brolin and R. Kádár, *Physics of Fluids*, 2024, **36**, year.

[72] N. H. M. Yusoff, C. H. Chong, Y. K. Wan, K. H. Cheah and V.-L. Wong, *Journal of Water Process Engineering*, 2023, **51**, 103410.

[73] S. P. Regalla, S. S. Karwa, S. Rajesh, P. Shyam and P. N. Shrivastava, *Materials Today: Proceedings*, 2020, **28**, 1030–1038.

[74] J. Koffler, W. Zhu, X. Qu, O. Platoshyn, J. N. Dulin, J. Brock, E. Graham, A. Luque, X. Zhong, E. Sakamoto, S. Marsala, M. Chen, Y. Zhong, X. Niu, J. Marsala, S. Chen, S. Sakamoto and S. B. Chen, *Nature Medicine*, 2019, **25**, 263–269.